Microfluidics and Nanofluidics (2023) 27:76
https://doi.org/10.1007/s10404-023-02685-w

RESEARCH

Stiffness influence on particle separation in polydimethylsiloxane-based deterministic lateral displacement devices

Julius Marhenke[1] · **Tobias Dirnecker**[1] · **Nicolas Vogel**[2] · **Mathias Rommel**[3]

Received: 5 May 2023 / Accepted: 13 September 2023 / Published online: 5 October 2023

Abstract
Polydimethylsiloxane (PDMS) is a popular material to rapidly manufacture microfluidic deterministic lateral displacement (DLD) devices for particle separation. However, manufacturing and operation challenges are encountered with decreasing device dimensions required to separate submicron particles. The smaller dimensions, notably, cause high hydraulic resistance, resulting in significant pressure even at relatively low throughputs. This high pressure can lead to PDMS deformation, which, in turn, influences the device performance. These effects may often be overlooked in the design and operation of devices but provide a systematic source of error and inaccuracies. This study focuses in detail on these effects and investigates pillar deformation in detail. Subsequently, we discuss a potential solution to this deformation using thermal annealing to stiffen the PDMS. We evaluate the influence of stiffness on the separation performance at elevated sample flow rates with submicron particles (0.45 and 0.97 µm diameter). An excellent separation performance at high throughput is successfully maintained in stiffer PDMS-based DLD devices, while the conventional devices showed decreased separation performance. However, the increased propensity for delamination constrains the maximal applicable throughput in stiffer devices. PDMS deformation measurements and numerical simulations are combined to derive an iterative model for calculating pressure distribution and PDMS deformation. Finally, the observed separation characteristics and encountered throughput constraints are explained with the iterative model. The results in this study underline the importance of considering pressure-induced effects for PDMS-based DLD devices, provide a potential mitigation of this effect, and introduce an approach for estimating pressure-induced deformation.

Keywords Deterministic lateral displacement (DLD) · Polydimethylsiloxane (PDMS) · Stiffness · Pressure · Deformation

1 Introduction

Deterministic lateral displacement (DLD) devices are microfluidic devices capable of separating particles with high resolution (Huang et al. 2004). DLD devices have been employed in several, mainly biomedical (McGrath et al. 2014; Salafi et al. 2019), application areas, including blood fractionation (Davis 2008; Inglis et al. 2008, 2011), circulating tumor cell separation (Jiang et al. 2017; Okano et al. 2015), and pathogen separation (Beech et al. 2018; Holm et al. 2011). In addition, the separation of droplets (Tottori et al. 2017; Tottori and Nisisako 2018) was performed with DLD devices. While studies already showed the separation of submicron (Marhenke et al. 2023; Tottori et al. 2020) and nanometer scale (Tottori et al. 2020; Zeming et al. 2016, 2018) particles down to 20 nm (Wunsch et al. 2016), DLD device manufacturing and operating is still challenging for submicron and nanometer particle separation (Hochstetter et al. 2020).

Manufacturing challenges arise from the required dimensions in the DLD devices, as structures in the same size range are required. While specialized processes, such as electron beam lithography (Wunsch et al. 2016), can pattern devices with extremely small dimensions, this technique

✉ Julius Marhenke
julius.marhenke@fau.de

[1] Friedrich-Alexander-Universität Erlangen-Nürnberg, Electron Devices, Cauerstraße 6, 91058 Erlangen, Germany

[2] Friedrich-Alexander-Universität Erlangen-Nürnberg, Institute of Particle Technology, Cauerstraße 4, 91058 Erlangen, Germany

[3] Fraunhofer Institute for Integrated Systems and Device Technology IISB, Schottkystraße 10, 91058 Erlangen, Germany

is very time-consuming, expensive, and requires access to clean room infrastructure. A widespread, well-established, faster, and cheaper manufacturing approach is based on a polydimethylsiloxane (PDMS) molding and replication process. Master structures for the molding process are usually generated by conventional photolithography.

Conventional photolithography allows the reliable fabrication of structures with dimensions around 1 µm sufficient for submicron particle separation (Marhenke et al. 2023). However, even these dimensions can cause operational challenges as the hydraulic resistance increases with decreasing dimensions within the device (Hochstetter et al. 2020). The high hydraulic resistance leads to higher pressures and, eventually, throughput limitations. The throughput limitations are caused by the deformation of the soft PDMS structures (Inglis 2010; Sollier et al. 2011), affecting particle separation performance. Inglis et al. (2010) showed that incorporating a glass slide near the PDMS structures could reduce pressure-induced deformation. However, the process requires manufacturer skill, and glass slide structuring, which can constrain specific applications or manufacturing of multilayer devices. A more straightforward process to reduce pressure-induced deformation could be increased PDMS stiffness through thermal treatments (Johnston et al. 2014; Kim et al. 2014; Moučka et al. 2021).

In this work, we explore how such a thermal stiffening process affects the performance of PDMS-based DLD devices. We focus on operation at high sample flow rates (up to 4 µl/min), where deformation becomes significant and has been previously shown in our group to influence device performance (Marhenke et al. 2023). First, we investigate an appropriate thermal treatment to tailor the PDMS stiffness. Subsequently, we characterize in detail how the applied flow rates cause deformation of the pillar arrays in our devices, particularly comparing standard and stiffened devices. Based on these insights, we rationalize the resulting device performance. Finally, we propose an iterative model to calculate the pressure distribution and PDMS pillar deformation along a DLD device to estimate the device performance based on the applied flow rate and the material properties.

2 Methods and experiments

2.1 Manufacturing of bulk PDMS samples for stiffness characterization

Bulk PDMS samples were prepared for stiffness determination. First, the PDMS (Sylgard™ 184, Dow Corporate, USA) was mixed in a 10:1 base component to curing agent weight ratio as recommended by the manufacturer. After mixing, the PDMS was degassed, poured into a mold, and cured in an oven under an ambient atmosphere. Curing was performed for 24 h at 50 °C, which we term standard PDMS. Finally, the bulk sample was cut out of the cured PDMS. The cylindrical bulk samples were roughly 10 mm in height and 20 mm in diameter. In total, three batches of PDMS were prepared.

A thermal treatment tuned the PDMS stiffness of the standard PDMS. The treatment duration was 2 h at 150 °C in an oven under an ambient atmosphere. PDMS after the thermal treatment is termed stiffened.

2.2 Mechanical characterization of bulk PDMS samples

A LRX Plus material testing machine (Lloyd Instruments, UK) was used to measure force–displacement curves. A probe compressed the bulk PDMS samples to a total force of 450 N. The displacement of the bulk PDMS sample was measured during compression. A preload of 1 N was applied to ensure contact between the PDMS and probe. Finally, the engineering stress was calculated as the applied force per sample cross-section area. The strain was calculated with the measured probe compression and PDMS bulk sample height. A linear fit from 0 to 10% strain was performed to obtain the Young's modulus (Moučka et al. 2021). Each of the three bulk PDMS samples was measured three times.

First, the stiffness of standard PDMS was obtained. Then, the thermal treatment to tune the stiffness was conducted, and the measurement was repeated for the treated samples.

2.3 Design of DLD devices

A detailed description of the used DLD device design is given in the supplementary information and Fig. S1. In short, the DLD devices consisted of an inlet region, outlet region, and pillar array. The inlet region had three inlets, two outer inlets for a buffer solution, and one central sample inlet. Each buffer inlet was connected by five equally sized channels (200 µm width) to the pillar array. In contrast, the sample inlet had one channel (200 µm width). The outlet region also had three outlets (1, 2, and 3). In outlet 1, large (displaced) particles, and in outlet 2, small particles should be collected. In outlet 3, no particles should be collected, and it was used to control proper device operation. Each outlet was connected to the pillar array by five equally sized channels (140 µm width).

Pillar rows perpendicular to the fluid flow direction are positioned in the pillar array. The pitch (pillar center-to-center distance) was 29 µm. Each subsequent row was offset by 1/50 toward the upper channel wall. Therefore, after 50 rows, the initial array arrangement is repeated, which is the periodicity (N) of the DLD device.

The pillar gap (G) was measured to be 2.7 µm after DLD devices molding. A theoretical, critical diameter can then be estimated based on the periodicity and pillar gap. Particles with a diameter above the critical diameter should be displaced (outlet 1), while smaller particles should not experience displacement (outlet 2).

The critical diameter was estimated based on a parabolic theory (Inglis et al. 2006) and a model proposed by Davis (2008) to be 0.48 µm (Eq. (1), $D_{c,P}$) and 0.58 µm (Eq. (2), $D_{c,D}$), respectively. The parameter η, accommodating non-uniform flow through the pillar gap (Inglis et al. 2006), was estimated as 4.4 for calculation:

$$D_{c,P} = 2\eta G/N, \tag{1}$$

$$D_{c,D} = 1.4GN^{-0.48}. \tag{2}$$

2.4 Manufacturing of DLD devices

The same manufacturing process as described in Marhenke et al. (2023) was used. However, a new master wafer was prepared for this study, and slight differences in pillar gap and device height were obtained.

The master wafer manufacturing process is summarized as follows. First, a 150 mm silicon wafer was spin-coated with SU-8 2050 (MicroChem, U.S.A.) photoresist at 4000 rpm for 60 s. An MA6 mask aligner (Süss GmbH, Germany) lithography system equipped with an i-line filter to ensure vertical side walls (Campo and Greiner 2007) was used for exposure. The final thickness, measured with a P-16 + stylus profilometer (KLA-Tencor, USA), was 32.16 ± 1.25 µm.

PDMS (Sylgard™ 184, Dow Corporate, USA), used for DLD device molding, was prepared and cured the same way as the bulk samples. The two-step approach of curing and followed thermal treatment was chosen as increased Young's modulus could prevent peeling the PDMS off the master wafer, as it was reported for a stiffer PDMS type (h-PDMS) by Inglis (2010). First, the cured PDMS was peeled off the SU-8 master wafer, individual devices were cut out, and holes for inlets and outlets were structured with a 1.5 mm biopsy punch. Then, the PDMS was permanently bonded to a glass slide by plasma treatment (30 s at 100 W) with an argon and oxygen mixture.

Besides the standard PDMS devices, devices with the additional thermal treatment of 2 h at 150 °C were manufactured. The additional thermal treatment was performed before or after bonding to investigate the influence of the additional thermal treatment on the final devices.

2.5 Operation of DLD devices and particle separation characterization

The DLD devices were operated with two Fusion 100 syringe pumps (Chemyx, U.S.A.). DI water with 1 vol.% Tween-20 (Sigma-Aldrich, USA) was used as buffer fluid to prevent clogging. The separation performance was evaluated with 0.45 ± 0.10 µm and 0.97 ± 0.03 µm polystyrene particles (Microparticles GmbH, Germany). The 0.45 µm particles were labeled with a green pyrromethene fluorescent dye, and the 0.97 µm particles were labeled with a red squaraine fluorescent dye. Based on Eqs. (1) and (2), the 0.45 µm particles should not be displaced in the DLD devices. Hence, the 0.45 µm particles should be collected in outlet 2 while the 0.97 µm particles should be displaced into outlet 1. The purchased particle solutions (2.5 wt.%) were diluted by adding 0.5 µl of the 0.45 µm and 0.75 µl of the 0.97 µm particle solution into 5 ml of buffer fluid.

First, the two buffer inlets were connected by inserting tubing into the inlet holes for device priming. The buffer syringe pump was operated at 2.5 µl/min until the buffer fluid filled the inlet region of the DLD device. Then, the sample was connected to the DLD device by inserting the tubing into the sample inlet. The sample syringe pump was operated at one-fifth (0.5 µl/min) of the buffer flow rate, as a uniform flow profile into the pillar array is desired. Any remaining air bubbles in the outlet region of the DLD devices were pushed out with a flat spatula. After that, the DLD device was put in a confocal fluorescence microscope TCS SP5 (Leica, Germany). Short videos (~ 10 s) of the outlets were recorded. After video recording, the flow rate was increased. The DLD devices were equilibrated for roughly 5 min before the next set of videos was recorded. The applied sample flow rates were 0.5, 1, 2, 3, and 4 µl/min with the corresponding buffer flow rates of 2.5, 5, 10, 15, and 20 µl/min. A detailed description of the video recording and analysis is given in the supplementary information.

The recorded videos were then analyzed with Fiji (Schindelin et al. 2012) to determine the fraction of particles displaced into outlet 1. A displacement efficiency was determined by the measured fluorescence intensity of a particular particle size in outlet 1 divided by the total fluorescence intensity of the same particular particle size in outlets 1 and 2. The definition is also given in supplementary eq. S1. A good separation of differently sized particles is achieved when particles above the critical diameter exhibit a high displacement efficiency while smaller particles exhibit a low displacement efficiency. As no particles were observed in outlet 3, the videos from outlet 3 were used to check the DLD devices' correct operation and subtract detector noise.

2.6 Numerical simulations of pillar arrays

One array period of 50 pillar rows was modeled and simulated in COMSOL Multiphysics® 6.0 to estimate the applied pressure. Each row consisted of 85 pillars. The pillar pitch was kept constant at 29 µm. As pressure-induced pillar deformation was expected, pillar arrays with pillar diameters of 26 to 22 µm (0.5 µm steps) were simulated.

Laminar flow, no-slip condition, and incompressible fluid were assumed for the simulations. As the used simulation model with more than 4000 pillars was already complex, 2D simulations were performed. However, a shallow channel approximation was used to consider the device height of 32 µm. Further, the simulated pillar gaps were much narrower than the device height, so the device height should not be a dominant factor under these conditions (Davis 2008).

The relative pillar gap and height changes due to deformation were also approximated. To assess the relative contributions of both factors to the device performance, we estimated the relative changes in these parameters as a function of pillar diameter. We assumed a constant pillar volume for this estimation due to the 0.5 Poisson ratio of PDMS (Johnston et al. 2014). In the case of a device having a pillar diameter of 26.3 µm, a height of 32.2 µm, and a gap of 2.7 µm, which is the case of the used devices, a pillar diameter reduction of 1 µm results in a merely 8.1% height increase while the pillar gap increases by 37.0%. The calculation is shown in the supplementary information.

Inlet velocities of 1, 3, 5, 7, 9, and 11 mm/s were specified for the simulations. These values cover the range of applied flow rates during experimentation. The velocity-to-flow rate conversion was performed by multiplying the velocity with the channel cross-section.

In the end, the pressure drop along the array period was determined for each inlet velocity and used to calculate the hydraulic resistance of a pillar array with the respective pillar gap. The outlet was set to atmospheric pressure for all simulations.

3 Results and discussion

3.1 Stiffness characterization of bulk PDMS samples

First, the Young's modulus of bulk PDMS samples was characterized. The obtained Young's moduli and exemplary stress–strain curves for standard and stiffened PDMS samples are shown in Fig. 1.

The Young's modulus of the standard PDMS was 2.00 ± 0.09 MPa and increased to 3.38 ± 0.13 MPa for the stiffened PDMS, respectively. Therefore, the thermal treatment could successfully alter the Young's modulus. The measured values are also in accordance with the literature values (1.32 to 2.97 MPa (Johnston et al. 2014) and 1.32 to 4.42 MPa (Moučka et al. 2021)).

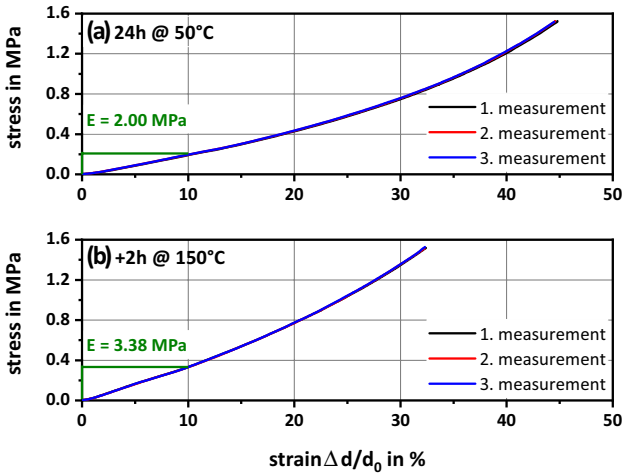

Fig. 1 Stress–strain curves of **a** standard (24 h at 50 °C) and **b** stiffened (+2 h at 150 °C) PDMS samples. The Young's moduli (*E*) were determined in a 0 to 10% strain regime

Besides the 2 h at 150 °C, a second thermal treatment for another 68 h at 150 °C was performed to investigate whether treatment time can further control the stiffening effect. However, only a minor Young's modulus increase to 3.72 ± 0.05 MPa was determined. Second, we used a third treatment step at a higher temperature (2 h at 250 °C), ultimately decreasing Young's modulus to 3.01 ± 0.09 MPa. Therefore, we used the annealing protocol of 2 h at 150 °C in all further experiments, as it yielded the highest Young's modulus increase over a practical short treatment time. The Young's modulus values for all treatments are shown in Figure S3.

3.2 Operation of DLD devices

Next, the operation of DLD devices was evaluated. Three standard (24 h at 50 °C) and six stiffened DLD devices were prepared. Three devices were annealed at 150 °C for 2 h before bonding to a glass slide, while the other set was first bonded to the glass slide and subsequently annealed. The standard devices were operated at sample flow rates of 0.5, 1, 2, 3, and 4 µl/min without complication. In addition, continuous operation of a device for more than 1 h at 4 µl/min was possible without showing any indication of delamination. However, the inlet structuring process had to be adjusted for the stiffened devices as tube insertion caused rupturing of PDMS. First, a biopsy punch with a diameter of 2.0 mm instead of 1.5 mm was used. However, the previously used low-density polyethylene (LDPE) tubing (1.8 mm outer diameter) did not yield a reliable and tight connection. Therefore, a small piece of polyvinyl chloride (PVC) tubing

(2.1 mm outer diameter) was fitted over the PVC tubing before insertion into the inlet hole. This approach prevented PDMS rupture and leaking inlets.

Furthermore, it was noticed that devices stiffened after bonding tended to fail at sample flow rates between 2 and 3 µl/min by delamination from the glass slide. The operation of devices stiffened before bonding was reliably possible up to 3 µl/min sample flow rate. One of the three devices could also be run at 4 µl/min without delamination. The thermal treatment seems to weaken the bond to the underlying glass substrate. In the following, we only use devices stiffened before the bonding process.

3.3 Separation characteristics of DLD devices

Standard and stiffened devices were operated with 0.45 and 0.97 µm particles for separation performance evaluation. The obtained displacement efficiencies are shown in Fig. 2.

At the lower sample flow rates of 0.5 and 1.0 µl/min, reliable separation of the 0.45 and 0.97 µm particles was achieved with a complete displacement of the 0.97 µm particles into outlet 1 and only small quantities of displaced 0.45 µm particles. The displacement efficiency of 0.45 µm particles seemed unaffected by increasing flow rates. However, when evaluating the recorded videos by eye, it seems that agglomerates of 0.45 µm particles, much larger than a single particle, were the primary cause for the measured signal in outlet 1. Therefore, the low signal of displaced particles can be attributed to problems in the colloidal dispersion and is not caused by malfunction of the devices.

For the standard devices, the displacement efficiency of the 0.97 µm dropped to 91.5 ± 6.0% at 2.0 µl/min sample flow rate. Further sample flow rate increase to 3.0 and 4.0 µl/min resulted in continued displacement efficiency decrease to 68.7 ± 6.0 and 54.4 ± 1.6%, respectively. In the case of stiffened devices, the displacement efficiency at 2.0 µl/min sample flow rate was still at 98.9 ± 1.1% and dropped to 94.4 ± 3.4% at 3.0 µl/min. Even at the highest sample flow rate of 4.0 µl/min, a displacement efficiency of 93.4% was determined. However, only one of the three stiffened devices could be operated at the highest investigated flow rate (Fig. 2), while the other devices failed due to delamination. These experiments indicate that stiffened devices showed higher displacement efficiencies at elevated flow rates compared to the standard devices but at the expense of a more limited maximum flow rate.

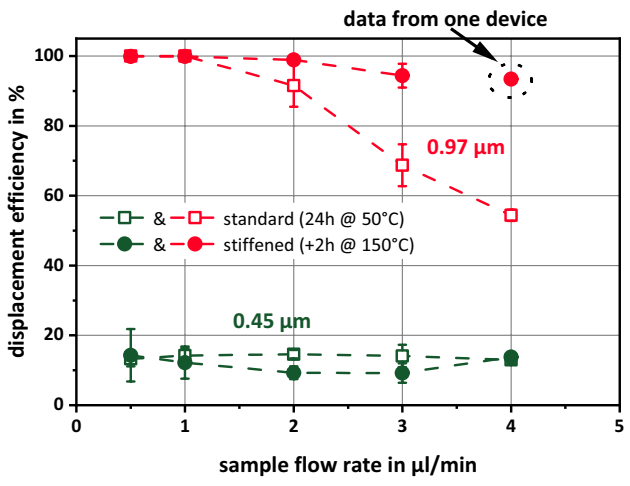

Fig. 2 Determined displacement efficiencies of 0.45 and 0.97 µm particles in standard ($n = 3$) and before bonding stiffened ($n = 3$) DLD devices at different sample flow rates

In addition, Reynolds numbers for all experiments were calculated to characterize the fluid dynamics within our microfluidic devices. At Reynolds numbers above 10, alterations of particle displacement in DLD devices were previously reported (Dincau et al. 2018; Wullenweber et al. 2022) and may be an additional cause for the altered displacement efficiencies at higher flow rates, in addition to the geometric deformations. For the calculations, the flow speed was estimated based on the applied flow rate and device geometry (Marhenke et al. 2023). For the highest applied flow rate of 4 µl/min, a Reynolds number of 0.5 was found. Since the calculated Reynolds number is still below 1 for all cases, the increased Reynolds number is unlikely to be the origin of the observed decrease in displacement efficiency.

Further, optical microscopy was then used to investigate the origin of standard devices' decreased performance and an increased propensity for delamination of stiffened devices at the highest sample flow rate.

3.4 Deformation of PDMS pillars

A standard and a stiffened device were operated in a microscope to observe the inlet and outlet region in detail. The pillar gaps at the inlet and outlet were obtained from images and are shown in Fig. 3.

The pillar gap of devices before bonding was measured to be 2.7 µm and, as such, was assumed for no flow condition (0.0 µl/min). The pillar gaps at the outlet tended to be stable around 2.7 to 2.8 µm for the applied flow rates, especially for the stiffened device. The standard device exhibited slightly increased outlet pillar gaps at 3 and 4 µl/min. In addition, significant pillar compression was observed at the inlet region, which increased with increasing flow rates and was more pronounced in standard devices.

At 2 µl/min sample flow rate, the inlet pillar gap for standard devices was 6.4 µm correlating to critical diameters of 1.13 and 1.37 µm based on Eqs. (1) and (2). Both calculated critical diameters are above the 0.97 µm particles. Hence, a displacement efficiency deterioration was observed. Furthermore, the inlet pillar gap widened with continued flow rate

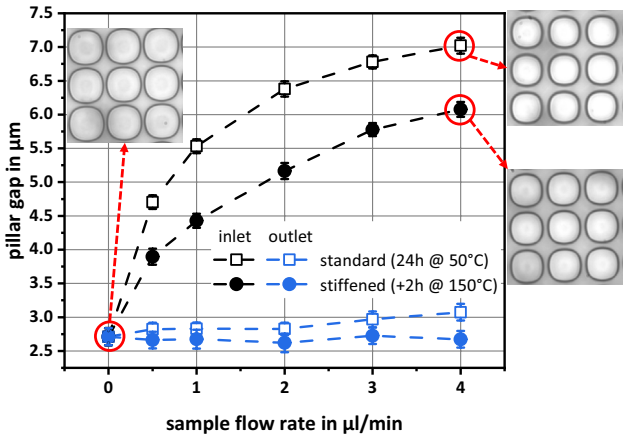

Fig. 3 Measured pillar gaps near the inlet and outlet for standard and stiffened DLD devices at different sample flow rates. Insets show exemplary pictures of pillars in different conditions

increases, and further displacement efficiency deterioration was encountered.

In contrast, the stiffened device only showed an inlet pillar gap of 6.1 µm at the highest sample flow rate (4 µl/min). The corresponding critical diameter were 1.10 and 1.30 µm (Eqs. (1) and (2)). These values are also slightly above the 0.97 µm particles. However, the pillar gap change is smaller than for standard devices, so the displacement efficiency deterioration is also lower. Therefore, the stiffening reduced pillar deformation and preserved better device performance at high flow rates.

In addition, a mechanical simulation of the pillar deformation was performed to evaluate the height-dependent deformation behavior. Three stages (small, medium, and strong deformation) were simulated to evaluate deformation along pillar height. Generally, the deformation was uniform with less than 10% deformation deviation except for regions close to the pillar's bottom or top. The supplementary information and Fig. S4 include more details concerning the mechanical simulation. Based on these insights, we approximate the pillar deformation to be uniform along the entire height to simplify our arguments.

Ultimately, the observed displacement efficiency deterioration with increasing flow rate is assumed to be connected to the pillar gap broadening. The relationship between pillar deformation and flow rate is investigated more thoroughly in the following.

3.5 Pressure and pillar gap calculation

We use numerical simulations to correlate the pressure within the device with the pillar gap broadening. First, we calculate the pressure drop (Δp) along a DLD array based on the total flow rate (Q) and the hydraulic resistance (R) (Sollier et al. 2011; Tottori et al. 2020):

$$\Delta p = Q \cdot R. \tag{3}$$

The total flow rate was the sample flow rate plus twice the buffer flow rate and could be directly controlled with the syringe pumps. The hydraulic resistance, as a function of various pillar gaps, was obtained from the numerical simulations, as detailed in the supplementary information.

A power law fit to the individual data points (Fig. S5) yielded an expression to calculate the hydraulic resistance $R_p(G)$ (in Pa·s/µm^3) of one pillar array period as a function of the pillar gap G (in µm):

$$R_p(G) = 1.01 \cdot 10^{-3} \cdot G^{-2.45}. \tag{4}$$

The total hydraulic resistance of a device ($R_d(G)$) can then be obtained by multiplying the calculated value from Eq. (4) by the total number of periods (N_p) (Tottori et al. 2020) as in Eq. (5):

$$R_d(G) = R_p(G) \cdot N_p. \tag{5}$$

The total number of periods in the used devices was 29. From $R_d(G)$, the pressure drop can then be calculated according to Eq. (3). However, as the pillar gaps varied along the device (Fig. 3), a position-dependent pillar array resistance must be considered for the pressure calculation.

First, the total pillar array length (42.05 mm) was discretized into 100 µm segments. The chosen segment size should be sufficiently fine as no significant pillar gap broadening was observed within individual microscopy images covering roughly 285 µm. Then the pillar gap was calculated for each segment, assuming a linear change along the array (Fig. 4a, denoted by "lin. assumption"). Finally, the hydraulic resistance was calculated for each segment. Multiplying the hydraulic resistance and total flow rate yields the pressure contribution of the corresponding discretized segment (Eq. (3)).

The local pressure at a given position can then be calculated by summation of the subsequent discretized segments. For example, previous segments do not influence the local pressure in the last segment (420th) before the outlet. However, the local pressure in the preceding segment (419th) consists of the 420th and 419th segment's pressure contribution. With this procedure, the local pressure along the pillar array was obtained (Fig. 4b, denoted by "calculation").

Building on the knowledge of the local pressure, the pillar deformation was calculated for each discretized element. The calculated local pressure was taken as the applied stress to obtain the corresponding pillar strain. A third-order polynomial fit was used to describe the stress–strain relation in Fig. 1. However, comparing the calculated (Fig. 4a, denoted by "calculation") and initially assumed pillar gaps for the

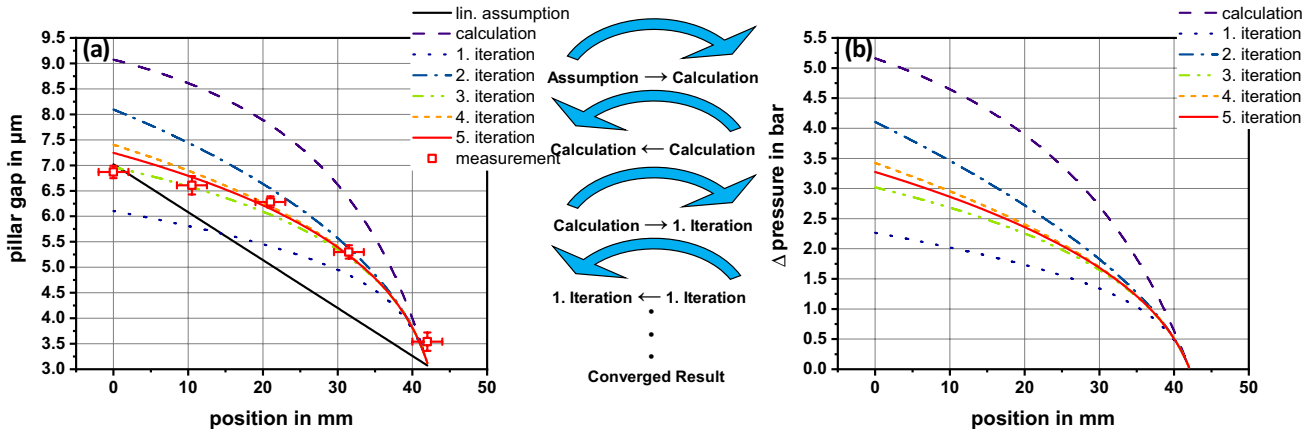

Fig. 4 Estimated **a** local pillar gaps and **b** pressure distribution along the pillar array (inlet to outlet) in a standard (24 h at 50 °C) DLD device operated at a 4 µl/min sample flow rate. In **a** also, measured pillar gaps along the DLD device position are shown

calculation of the local pressure (Fig. 4a, denoted by "lin. assumption") showed significantly different characteristics. Therefore, based on the calculated local pillar gaps, the pressure distribution was re-calculated (Fig. 4b, denoted by "1. iteration"). Then, the local pillar gaps were again re-calculated (Fig. 4a, denoted by "1. iteration") using this iterated pressure distribution. This iterative procedure was repeated until the results converged, achieved after 5 iterations.

The local pillar deformations were experimentally determined to verify the results of the iterated calculations. A standard DLD device was operated at 4 µl/min in a microscope, and images of different pillar array areas along the pillar array were taken. A ruler was used to determine the inner position in the pillar array, with an approximate uncertainty of ± 2 mm. The measured pillar gaps at five locations across the pillar array (Fig. 4a, denoted by "measurement") verified that the decrease in pillar gaps was as predicted by the iterated model calculations.

Given the experimental uncertainties in determining local position as well as the exact pillar gap from the microscopy images, the experimental results corroborate with the values determined by the iterative model.

The iterative model calculations provided a possible explanation for the observed differences in maximum flow rate for standard and stiffened devices. Based on the iterative model, the pressure drop in a standard device was calculated to be 3.3 bar at a 4 µl/min sample flow rate (Fig. S6a). For the stiffened devices, the calculated pressure drop was 4.1 to 4.8 bar for 3 and 4 µl/min sample flow rates (Fig. S6b), respectively. This pressure difference is caused by the different propensity of the pillars to deform and, thus, the different hydraulic resistances.

The standard devices were all operated at the maximum flow rate (4 µl/min), while two out of three stiffened devices failed at this flow rate and delaminated from the substrate. This difference in operation capabilities is caused by the significantly increased pressure in the stiffened devices. In literature, a wide range for pressure-induced delamination is reported, with an approximate range of 2.1 to 4.8 bar (30 to 70 psi) (Sollier et al. 2011). While the observed delamination occurs at the higher end of the reported literature values, the calculated values are still within limits.

3.6 Estimation of effective displacement length

The calculated position-dependent pillar gaps were further used to estimate the theoretical displacement behavior for comparison with measurements. No changes in displacement efficiency for the 0.45 µm particles were expected as the critical diameter of the DLD devices was already above the particle diameter and shifted further upwards for higher flow rates. This assumption is also supported by the data shown in Fig. 2, as the change in flow rate hardly influenced the displacement efficiency of the 0.45 µm particles.

The critical pillar gap for the displacement of 0.97 µm particles was estimated as 5.51 (Parabolic) and 4.53 µm (Davis) with Eqs. (1) and (2), respectively. Then, the array length with pillar gaps below the critical pillar gap (effective displacement length) was determined from the iterative model calculations (Fig. S6c, d). The results are summarized in Table 1.

We assume a complete displacement of the 0.97 µm particles along the (calculated) effective displacement length. This assumption means that the particles perfectly follow the pillar array direction toward outlet 1 for the effective displacement length. With the array periodicity and effective displacement length (l), the theoretically expected lateral displacement distance (Δy) from the sample inlet position toward outlet 1 at the end of the pillar array was calculated:

Table 1 Effective displacement length in standard (24 h at 50 °C) and stiffened (+2 h at 150 °C) DLD devices at different flow rates

Device	Model	Sample flow rate in µl/min				
		0.5	1.0	2.0	3.0	4.0
Standard	Parabolic	42.05 mm	42.05 mm	27.65 mm	18.05 mm	13.25 mm
	Davis	42.05 mm	23.85 mm	11.85 mm	7.55 mm	5.45 mm
Stiffened	Parabolic	42.05 mm	42.05 mm	42.05 mm	33.85 mm	25.65 mm
	Davis	42.05 mm	42.05 mm	22.85 mm	14.45 mm	10.95 mm

The maximal possible displacement length is 42.05 mm

$$\Delta y = l/N. \tag{6}$$

We experimentally assessed the displacement efficiency using videos taken in the fluorescence microscope where the stream of fluorescent particles was visible (Fig. 5). Measuring the position of this particle stream enables us to determine a weighted mean displacement distance value as a function of the different applied flow rates. In addition, a weighted standard deviation of the outlet particle positions was calculated. For both calculations, the measured fluorescence intensity at the different positions in the outlet channels was used for weighting. The experimentally and theoretically obtained lateral displacement distances are shown in Fig. 5. As the sample inlet is 200 µm wide, the theoretically expected lateral displacement distances are also spread over this distance. Any broadening of the displacement by diffusion, particle–particle interactions, or particle-pillar interactions was neglected. In addition, depending on the method used to calculate the critical pillar gap (Parabolic vs. Davis), different effective displacement lengths resulted,

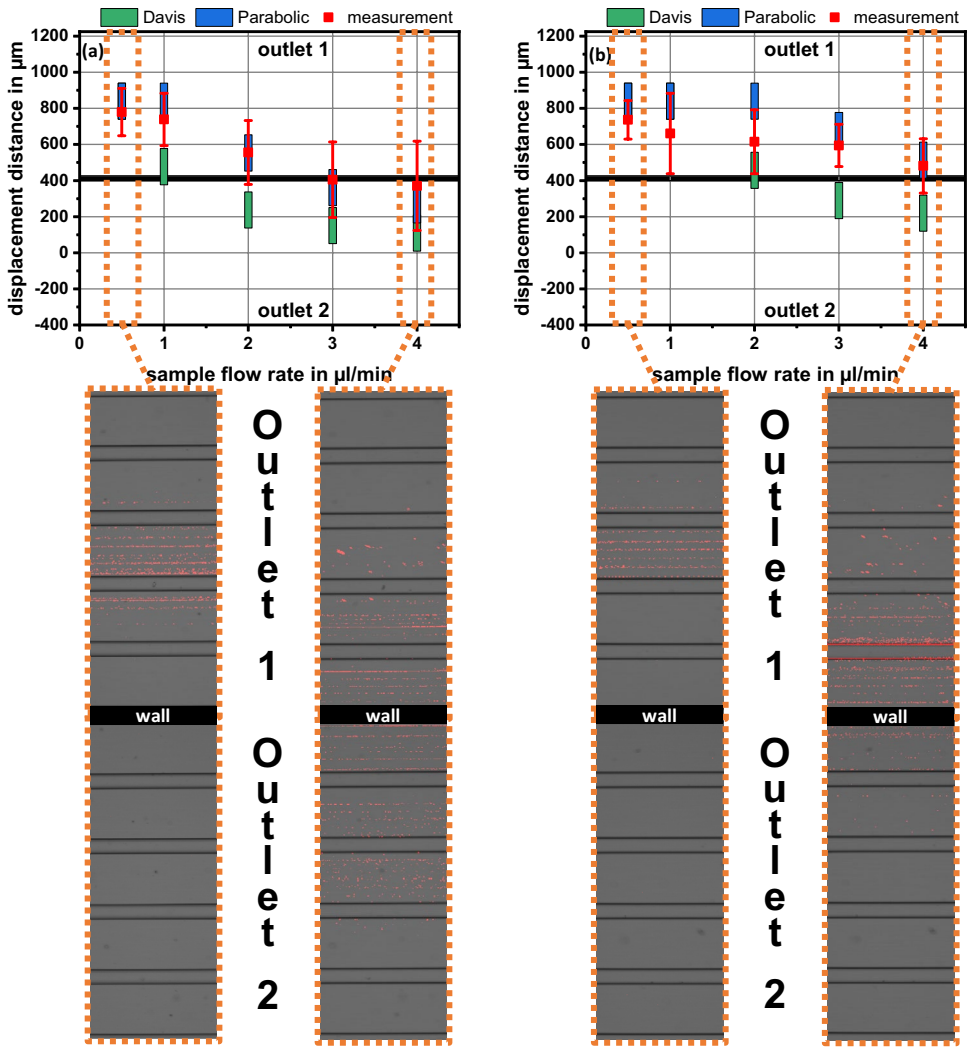

Fig. 5 Theoretically (Parabolic and Davis) and experimentally obtained lateral displacement distances for **a** standard and **b** stiffened DLD devices at different flow rates. The horizontal lines between 400 to 425 µm represent the wall separating outlets 1 and 2. Exemplary images of outlets 1 and 2 with the 0.97 µm particles at 0.5 and 4.0 µl/min sample flow rates in standard and stiffened devices are also shown. The captured videos were overlaid for better visualization to obtain exemplary images. A detailed description of video capturing and evaluation can be found in the supplementary information and Fig. S2

reflected in different total displacement distances (blue and green bars, respectively).

Generally, the experimentally determined lateral displacement distances agreed with the model's predictions. The decreases in experimental and theoretical lateral displacement distances were more pronounced in the standard devices compared to the stiffened ones, reflecting the decreased separation efficiencies observed in Fig. 2. In summary, the PDMS stiffening reduced the deformation of pillars in the applied DLD devices effectively and thus facilitated the separation of 0.97 µm particles at elevated flow rates, and thus, with higher overall throughput.

4 Conclusion

In this article, we demonstrate that device deformation can change the displacement efficiencies and, thus, the performance of DLD devices. We propose that PDMS stiffening can be used to enhance performance by suppressing such deformations. However, the flow rate may have to be reduced since delamination may cause device failure.

Based on the described iterative approach, expectable pressure and pillar deformation in devices could also be estimated to check the design's feasibility. Further, the effective displacement length of a device can be estimated so that a shorter device could achieve the same separation result but at lower pressure in the inlet. The lower inlet pressure would render delamination less probable, increasing device reliability. Finally, accurate determination of the deformation could be used to retro-engineer the device so that the deformation yields suitable displacements of a targeted particle system.

Supplementary Information The online version contains supplementary material available at https://doi.org/10.1007/s10404-023-02685-w.

Author contributions TD, NV, and MR supervised the work and reviewed and edited the manuscript. JM performed the experimental work and visualization of data and wrote the initial draft of the manuscript.

Funding Open Access funding enabled and organized by Projekt DEAL.

Data availability Data sets generated in this work are available from the corresponding author on reasonable request.

Declarations

Conflict of interest The authors declare that they have no conflicts of interest.

References

Beech JP, Ho BD, Garriss G, Oliveira V, Henriques-Normark B, Tegenfeldt JO (2018) Separation of pathogenic bacteria by chain length. Anal Chim Acta 1000:223–231. https://doi.org/10.1016/j.aca.2017.11.050

Campo Ad, Greiner C (2007) SU-8: a photoresist for high-aspect-ratio and 3D submicron lithography. J Micromech Microeng 17:R81–R95. https://doi.org/10.1088/0960-1317/17/6/R01

Davis JA (2008) Microfluidic Separation of Blood Components through Deterministic Lateral Displacement. PhD thesis, Princeton University

Dincau BM, Aghilinejad A, Hammersley T, Chen X, Kim J-H (2018) Deterministic lateral displacement (DLD) in the high Reynolds number regime: high-throughput and dynamic separation characteristics. Microfluid Nanofluid. https://doi.org/10.1007/s10404-018-2078-9

Hochstetter A, Vernekar R, Austin RH, Becker H, Beech JP, Fedosov DA, Gompper G, Kim S-C, Smith JT, Stolovitzky G, Tegenfeldt JO, Wunsch BH, Zeming KK, Krüger T, Inglis DW (2020) Deterministic lateral displacement: challenges and perspectives. ACS Nano 14:10784–10795. https://doi.org/10.1021/acsnano.0c05186

Holm SH, Beech JP, Barrett MP, Tegenfeldt JO (2011) Separation of parasites from human blood using deterministic lateral displacement. Lab Chip 11:1326–1332. https://doi.org/10.1039/c0lc00560f

Huang LR, Cox EC, Austin RH, Sturm JC (2004) Continuous particle separation through deterministic lateral displacement. Science 304:987–990. https://doi.org/10.1126/science.1094567

Inglis DW (2010) A method for reducing pressure-induced deformation in silicone microfluidics. Biomicrofluidics. https://doi.org/10.1063/1.3431715

Inglis DW, Davis JA, Austin RH, Sturm JC (2006) Critical particle size for fractionation by deterministic lateral displacement. Lab Chip 6:655–658. https://doi.org/10.1039/b515371a

Inglis DW, Morton KJ, Davis JA, Zieziulewicz TJ, Lawrence DA, Austin RH, Sturm JC (2008) Microfluidic device for label-free measurement of platelet activation. Lab Chip 8:925–931. https://doi.org/10.1039/b800721g

Inglis DW, Lord M, Nordon RE (2011) Scaling deterministic lateral displacement arrays for high throughput and dilution-free enrichment of leukocytes. J Micromech Microeng 21:54024. https://doi.org/10.1088/0960-1317/21/5/054024

Jiang J, Zhao H, Shu W, Tian J, Huang Y, Song Y, Wang R, Li E, Slamon D, Hou D, Du X, Zhang L, Chen Y, Wang Q (2017) An integrated microfluidic device for rapid and high-sensitivity analysis of circulating tumor cells. Sci Rep 7:42612. https://doi.org/10.1038/srep42612

Johnston ID, McCluskey DK, Tan CKL, Tracey MC (2014) Mechanical characterization of bulk Sylgard 184 for microfluidics and microengineering. J Micromech Microeng 24:35017. https://doi.org/10.1088/0960-1317/24/3/035017

Kim M, Huang Y, Choi K, Hidrovo CH (2014) The improved resistance of PDMS to pressure-induced deformation and chemical solvent swelling for microfluidic devices. Microelectron Eng 124:66–75. https://doi.org/10.1016/j.mee.2014.04.041

Marhenke J, Dirnecker T, Vogel N, Rommel M (2023) Increasing flow rates in polydimethylsiloxane-based deterministic lateral displacement devices for sub-micrometer particle separation. Microfluid Nanofluid. https://doi.org/10.1007/s10404-022-02609-0

McGrath J, Jimenez M, Bridle H (2014) Deterministic lateral displacement for particle separation: a review. Lab Chip 14:4139–4158. https://doi.org/10.1039/c4lc00939h

Moučka R, Sedlačík M, Osička J, Pata V (2021) Mechanical properties of bulk Sylgard 184 and its extension with silicone oil. Sci Rep 11:19090. https://doi.org/10.1038/s41598-021-98694-2

Okano H, Konishi T, Suzuki T, Suzuki T, Ariyasu S, Aoki S, Abe R, Hayase M (2015) Enrichment of circulating tumor cells in tumor-bearing mouse blood by a deterministic lateral displacement microfluidic device. Biomed Microdevices 17:9964. https://doi.org/10.1007/s10544-015-9964-7

Salafi T, Zhang Y, Zhang Y (2019) A review on deterministic lateral displacement for particle separation and detection. Nanomicro Lett 11:77. https://doi.org/10.1007/s40820-019-0308-7

Schindelin J, Arganda-Carreras I, Frise E, Kaynig V, Longair M, Pietzsch T, Preibisch S, Rueden C, Saalfeld S, Schmid B, Tinevez J-Y, White DJ, Hartenstein V, Eliceiri K, Tomancak P, Cardona A (2012) Fiji: an open-source platform for biological-image analysis. Nat Methods 9:676–682. https://doi.org/10.1038/nmeth.2019

Sollier E, Murray C, Maoddi P, Di Carlo D (2011) Rapid prototyping polymers for microfluidic devices and high pressure injections. Lab Chip 11:3752–3765. https://doi.org/10.1039/c1lc20514e

Tottori N, Nisisako T (2018) High-throughput production of satellite-free droplets through a parallelized microfluidic deterministic lateral displacement device. Sens Actuators, B Chem 260:918–926. https://doi.org/10.1016/j.snb.2018.01.112

Tottori N, Hatsuzawa T, Nisisako T (2017) Separation of main and satellite droplets in a deterministic lateral displacement microfluidic device. RSC Adv 7:35516–35524. https://doi.org/10.1039/C7RA05852G

Tottori N, Muramoto Y, Sakai H, Nisisako T (2020) Nanoparticle separation through deterministic lateral displacement arrays in poly(dimethylsiloxane). J Chem Eng Japan / JCEJ 53:414–421. https://doi.org/10.1252/jcej.19we160

Wullenweber MS, Kottmeier J, Kampen I, Dietzel A, Kwade A (2022) Simulative investigation of different DLD microsystem designs with increased reynolds numbers using a two-way coupled IBM-CFD/6-DOF approach. Processes 10:403. https://doi.org/10.3390/pr10020403

Wunsch BH, Smith JT, Gifford SM, Wang C, Brink M, Bruce RL, Austin RH, Stolovitzky G, Astier Y (2016) Nanoscale lateral displacement arrays for the separation of exosomes and colloids down to 20 nm. Nat Nanotechnol 11:936–940. https://doi.org/10.1038/nnano.2016.134

Zeming KK, Thakor NV, Zhang Y, Chen C-H (2016) Real-time modulated nanoparticle separation with an ultra-large dynamic range. Lab Chip 16:75–85. https://doi.org/10.1039/c5lc01051a

Zeming KK, Salafi T, Shikha S, Zhang Y (2018) Fluorescent label-free quantitative detection of nano-sized bioparticles using a pillar array. Nat Commun 9:1254. https://doi.org/10.1038/s41467-018-03596-z